



Time-resolved optical spectroscopy measurements of shocked liquid deuterium

J. E. Bailey,¹ M. D. Knudson,¹ A. L. Carlson,¹ G. S. Dunham,² M. P. Desjarlais,¹ D. L. Hanson,¹ and J. R. Asay¹

¹*Sandia National Laboratories, Albuquerque, New Mexico 87185-1196, USA*

²*K-Tech Corporation, Albuquerque, New Mexico 87123, USA*

(Received 24 January 2008; revised manuscript received 16 June 2008; published 21 October 2008)

Time-resolved optical spectroscopy has been used to measure the shock pressure steadiness, emissivity, and temperature of liquid deuterium shocked to 22–90 GPa. The shock was produced using magnetically accelerated flyer plate impact, and spectra were acquired with a suite of four fiber-optic-coupled spectrometers with streak camera detectors. The shock pressure changes by an average of -1.2% over the 10–30 ns cell transit time, determined from the relative changes in the shock front self-emission with time. The shock front reflectivity was measured from 5140 Å and 5320 Å laser light reflected from the D_2 shock. The emissivity inferred from the reflectivity measurements was in reasonably good agreement with quantum molecular dynamics simulation predictions. The spectral radiance wavelength dependence was found to agree well (average normalized $\chi^2=1.6$) with a Planckian multiplied by the emissivity. The shock front temperature was determined from the emissivity and the wavelength-dependent shock self-emission. Thirty-seven temperature measurements spanning the 22–90 GPa range were accumulated. The large number of temperature measurements enables a comparison of the scatter in the data with expectations for a Gaussian distribution. This facilitates determination of uncertainties that incorporate both apparatus contributions and otherwise unquantified systematic effects that cause self-emission variations from one experiment to another. Agreement between temperatures determined from the absolute spectral radiance and from the relative shape of the spectrum further substantiates the absence of systematic biases. The weighted mean temperature uncertainties were as low as $\pm 3\text{--}4\%$, enabling the discrimination between competing models for the D_2 equation of state (EOS). The temperature results agree well with models that predict a maximum compression of ~ 4.4 . Softer models that predict approximately sixfold compression are inconsistent with the data to a very high statistical confidence level. Previous analysis [D. Saumon and T. Guillot, *Astrophys. J.* **609**, 1170 (2004)] of Jupiter’s internal structure has shown that the core mass is restricted to be less than approximately three times the mass of the Earth, if EOS models consistent with these temperature measurements are employed.

DOI: [10.1103/PhysRevB.78.144107](https://doi.org/10.1103/PhysRevB.78.144107)

PACS number(s): 64.30.Jk, 62.50.Ef

I. INTRODUCTION

Warm dense matter is an active research area, bridging the traditional definitions of plasma physics and condensed matter physics. In this intermediate regime, mixtures of molecules, atoms, and ions exist. The mixture composition is important for understanding the equation of state (EOS), since dissociation and ionization affect the division between internal energy and thermal energy. In this paper we describe time-resolved optical spectroscopy measurements of shocked liquid deuterium that help discriminate between models that employ different approximations for the EOS.

The study of shocked liquid deuterium has been the focus of much research in recent years.^{1–3} Interest in this hydrogen isotope arises from two main sources. First, this atom is amenable to theoretical modeling by many different approaches.^{3–13} Despite the simple atomic structure, descriptions of the equation of state in the warm dense matter regime are complex and approximations are a necessity. Comparisons of models with data can help evaluate which model approaches are suitable for different regimes of the phase space. In addition, the approaches known as “chemical models” explicitly use experimental data to set adjustable parameters that influence the EOS results. The second reason is the importance of hydrogen and its isotopes for applications. The giant planets are believed to consist of hydrogen and helium at high pressure.^{14,15} A recent analysis of the internal struc-

ture of Jupiter and Saturn showed that the core mass and metallicity are strongly dependent on the EOS model.¹⁴ Laboratory experiments can help reduce the overall model uncertainties by reducing the uncertainty contribution due to the EOS. A major terrestrial application is the inertial confinement approach to thermonuclear fusion.¹⁶ This approach relies on shocking and compressing a cryogenic mixture of deuterium and tritium. The degree of compressibility affects the shock timing, final fuel density, and the fusion yield.

Shocked liquid deuterium EOS measurements have been performed using gas gun, laser, high explosive, and Z-pinch facilities. Gas gun experiments access relatively low pressures up to ~ 23 GPa, but were responsible for the first observations of the transformation of hydrogen from its insulating to metal-like state.¹⁷ Temperature measurements of gas gun multiply-shocked deuterium were lower than predictions, suggesting that deuterium was more compressible than expected.¹⁸ New EOS models were then proposed^{4,6,8} that predicted lower temperatures and higher compressions due to increased energy invested in dissociation. Laser experiments produced much higher pressures up to 230 GPa and appeared to confirm the higher compressions.^{19–22} Magnetically accelerated flyer impact experiments in the 20–100 GPa range contradicted the laser data and were consistent with less compressive (“stiffer”) EOS models.^{23–25} High explosive experiments²⁶ in similar regimes were also consistent with

stiffer models, as are some of the most recent laser experiments.²⁷

Measurements of the shocked D_2 temperature provide a significant constraint on EOS models. The underlying idea behind this sensitivity is appealingly simple: if more energy is invested in dissociation and ionization, then less energy is available to cause temperature increases. Lower temperature corresponds to higher compressibility. Thus, temperature and compressibility are interconnected with the details of the complex dissociation and ionization processes. The importance of temperature measurements is further elevated by the fact that dissociation and ionization are complicated to describe theoretically and no methods to directly measure shocked D_2 dissociation and ionization currently exist in this pressure regime.

Shocked deuterium temperature is inferred from combined measurements of the wavelength-dependent spectral radiance S_λ and the emissivity ε_λ . Assuming a Planck spectrum modified by ε_λ , the spectral radiance is $S_\lambda = \varepsilon_\lambda \{2\pi hc^2/\lambda^5\} \{\exp(hc/\lambda kT) - 1\}^{-1}$, where h is the Planck constant, c is the speed of light, λ is the wavelength, k is the Boltzmann constant, and T is the temperature. The gas gun work used a fiber-coupled six-channel photomultiplier tube pyrometer system^{18,28} to measure the spectral radiance. A simultaneous two-parameter fitting method was used to simultaneously constrain the emissivity and temperature using the absolute intensity and the spectral shape. Temperature measurements in laser shocked deuterium were performed²⁹ with a similar spectral radiance pyrometer diagnostic, augmented by emissivity values inferred from measurements of the shock front reflectivity.³⁰ Reflectivity measurements provide additional value because the transition from negligible reflectivity to moderately high values ($R \sim 0.5$) is considered a signature of the transition from an insulator to a metal-like state.^{12,30}

Time-resolved optical spectroscopy EOS measurements are extremely powerful: the shocked deuterium density, pressure, pressure steadiness, reflectivity/emissivity, and temperature can all be inferred from a single streaked spectrum. In the experiments described here, fiber-coupled streaked optical spectrometers^{31–33} record spectra from the rear side of a cryogenic D_2 cell shocked by magnetically accelerated flyer plate impact (Fig. 1). At shock pressures above ~ 20 GPa, the shocked D_2 is hot enough and optically thick enough to enable recording self-emission from the shock as it emerges from the Al pusher and propagates through the cell. The self-emission intensity as the shock propagates across the D_2 cell is related to the pressure and can be used to infer how constant the pressure is. The D_2 shock front emissivity and reflectivity can be determined from the intensity of laser light injected on adjacent fibers and reflected from the shock. The absolute wavelength-dependent spectral radiance can then be used to infer the shocked D_2 temperature.

When the shock reaches the rear of the D_2 cell, it reflects from the window and raises the temperature at the window/ D_2 interface to a higher value that depends on the reflected shock temperature and the interface cooling. Thus, the self-emission intensity can be used to infer the reflected shock temperature. This self-emission increase provides a signature of the time required for the shock to propagate

across the D_2 cell and thus infer the D_2 shock velocity. The inferred shock velocities ranged from 13–26 km/sec, in agreement with other measurements. The reflected shock travels back toward the moving Al/ D_2 interface and may be regarded as a probe for the size of the D_2 cell, similar to the role played by microwaves or laser light in radio detection and ranging (RADAR) or light detection and ranging (LIDAR) applications. When the reflected shock reaches the Al/ D_2 interface it reflects again, carrying information about the location of the Al/ D_2 interface back toward the window. The time between the first shock arrival at the D_2 /window interface and the subsequent reflected shock arrival can be used to infer the cell compression and singly shocked D_2 density.^{24,25} The shocked D_2 pressure can be inferred from the combined particle velocity and shock velocity measurements. Other diagnostics are available, and possibly superior, for some of these characteristics. In particular, velocity interferometer system for any reflector (VISAR) (Ref. 34) diagnostics provides direct shock velocity measurements with very high accuracy. Nevertheless, the ability to measure so many characteristics of the shocked D_2 with a single diagnostic merits attention.

The optical spectroscopy determinations of shock velocity and the use of shock reverberations to infer D_2 cell compression have been described in previous articles.^{23–25} In this paper we emphasize three measurements along the singly shocked D_2 Hugoniot: pressure steadiness inferred from the time-dependent self-emission, reflectivity/emissivity inferred from laser light reflected from the shock front, and shocked D_2 temperature inferred from the spectral radiance measurements. Work is in progress to infer the off-Hugoniot temperature conditions produced by the reflected shocks and will be reported in a future publication.

The results show that the pressure in these experiments was steady to within approximately -1% over the 10–30 ns initial shock transit through the D_2 cell. The measured emissivity was $\varepsilon = 0.91 \pm 0.04$ at 22 GPa and it fell to $\varepsilon = 0.7 \pm 0.05$ at 74 GPa. Quantum molecular dynamics simulations are in good agreement with the measured emissivity. Thirty-seven temperature measurements were obtained. This relatively large measurement collection enabled an evaluation of the measurement distribution, thereby providing the ability to quantitatively estimate the influence of systematic effects that cause variation in the measurement results. These systematic effects were included in the temperature uncertainties. The weighted mean temperature measurement accuracy, including uncertainty contributions from the apparatus, emissivity, and systematic effects, was conservatively estimated to be $\pm 3\text{--}6\%$ over $P = 22\text{--}42$ GPa, rising to $\pm 4\text{--}16\%$ over $P = 64\text{--}90$ GPa. Prior temperature measurements with gas gun and laser driven shocks are in reasonable agreement with the present measurements. The temperature accuracy is sufficient to quantitatively test EOS models using a chi-squared (χ^2) goodness of fit metric. We find that relatively stiff EOS models^{5,7,11,12} that predict a maximum compression of approximately four agree well with the data. The weighted mean normalized χ^2 for several of the stiff models based on quantum molecular-dynamics simulations is 0.5–1.2 over the 30–90-GPa range. The softer models^{4,6} that predict enhanced compression possess weighted mean normal-

ized χ^2 values that exceed ten and these models can therefore be excluded with high statistical confidence. The EOS models that agree with the temperature measurements lead to a predicted¹⁴ structure for Jupiter that consists of a relatively small core mass of approximately three times the mass of the Earth.

II. EXPERIMENT

The experiments were conducted using the Sandia National Laboratories Z facility³⁵ to produce a large magnetic pressure that accelerates planar Al or Ti flyer plates up to 22 km/s.³⁶ The magnetic pressure is generated^{37,38} by injecting ~ 20 MA peak current into a short circuit load that incorporates the flyer plate as one of the conductors (Fig. 1). The flyer impact onto a cryogenic cell launches a shock that reaches peak pressures of up to ~ 700 GPa in an Al pusher located on the front face of the cell. When the shock emerges into the liquid deuterium it generates shocks with 22–90-GPa pressures and shock velocities of 13–26 km/s. In some experiments²⁵ a flyer plate is incorporated into both sides of a rectangular power feed structure, enabling two separate cryogenic D_2 cells to be shocked in a single accelerator discharge (Fig. 1). The duration of the steady pressure phase can exceed 30 ns, limited by the effective flyer thickness at the moment of impact. Thicker, more massive flyers are slower, but they generate longer period of steady pressure. Steady pressure over cells with lateral dimensions ~ 5 mm promotes higher measurement accuracy and enables multiple simultaneous diagnostics. This technique has demonstrated the ability to achieve accuracies comparable to gas gun experiments, while reaching pressures up to six times higher.

The sample configuration is described in detail in Ref. 25. The D_2 thickness was 300–600 μm . The D_2 was condensed into the liquid phase using a cryostat especially designed³⁹ to cope with the stresses introduced by the delivery of ~ 10 MJ of electrical energy into a few cm^3 volume at the center of Z. The rear face of the cell was composed of sapphire (Al_2O_3), LiF, or quartz windows.

The diagnostics²⁵ used a collection of 16 fiber optics proximity coupled to the rear cell face to enable simultaneous VISAR,³⁴ shock break out (SBO),²⁵ and optical spectroscopy measurements.^{31–33} Each VISAR system used a frequency-doubled Nd:YAG laser injected into a “send” fiber to probe the reflective surface with 5320 \AA light. Each SBO system used a dye laser injected into another “send” fiber to probe the surface with 5140 \AA light. The use of these multiple techniques is significant for the optical spectroscopy described here both because they provide complementary information and because a small fraction of the laser light injected for the VISAR and SBO diagnostics is collected in the optical spectroscopy fibers after it reflects from the Al pusher or D_2 shock surface.

The four independent streaked spectrograph systems are described in Refs. 31–33. Light collected in a 200 μm or 400 μm core diameter fiber is transported 10–35 m from the cell to the spectrograph entrance. The spectrographs were either 1-m focal length and $f/7$ aperture or 2/3-m focal length with $f/4$ aperture. Blazed 150–300 g/mm gratings

provided 90–33 $\text{\AA}/\text{mm}$ dispersion. A streak camera with a 40-mm-long entrance slit placed in the spectrograph exit focal plane recorded time-resolved data over a 50–200 ns period. The system time resolution was determined by the fiber intermodal dispersion⁴⁰ and the streak camera resolution. The total resolution was 0.4–1.4 ns, depending on the streak camera sweep duration.³³

Typical time-resolved spectra are shown in Fig. 1. In this experiment three separate systems designated N19, N16, and N20 acquired two streaked spectra from one cell and a single spectrum from the other cell. The streak camera data are recorded on Kodak TMAX 400 film and the film response is unfolded using calibrated step wedges developed and scanned with the data. The time axis is applied using a comb output recorded either on the shot data itself or on associated calibration images. The wavelength scale was determined using wavelength fiducials applied by injecting light from HeNe and GreNe lasers. We corrected for the distortion caused by light propagation velocity variations with wavelength due to the refractive index changes with wavelength.⁴⁰ The streaked spectrograph systems, including the fiber optic input, the spectrograph, and the streak camera, were absolutely calibrated using a collection of light sources and NIST traceable detectors. The calibration methods are described in Ref. 33. The time history of the measured spectral radiance is shown in Fig. 2.

The spectral radiance rise time is potentially interesting because it may convey information regarding the shocked D_2 optical depth, transient kinetics, or electron-ion equilibration. The observed rise time (time to rise from 10% to 90% of the value reached during the steady emission phase) was approximately 5 ns at the lowest pressure (22 GPa), in good agreement with prior observations.¹⁸ The rise time at 31–90 GPa was approximately 2.2 ns, with a typical 1σ standard deviation of ± 0.7 ns. At these higher pressures there was no statistically significant rise time variation as a function of pressure or wavelength, and the rise time value was larger than the result reported in Ref. 29. The present experiments were designed to determine the entire time history of the initial and reflected shocks and the apparatus was not optimized for rise time measurements. Therefore, these observations may stimulate future research, but a detailed investigation was beyond the scope of the present work. As in Refs. 18 and 29, the pressure, emissivity, and temperature results presented below are restricted to the equilibrium conditions corresponding to the constant self-emission phase as the shock transits the bulk of the D_2 cell.

III. RESULTS: PRESSURE STEADINESS

The ability to produce 20–90 GPa shocks in liquid D_2 with 10–30 ns (or longer) steady pressure durations is a key feature of the magnetically accelerated flyer technique. Steady pressure is a fundamental assumption for the Rankine-Hugoniot equations that are commonly used for shock wave analysis to be valid. Steady pressure also greatly simplifies analysis of results obtained from reflected shock observations. The pressure variation with time in these experiments was determined from the measured time depen-

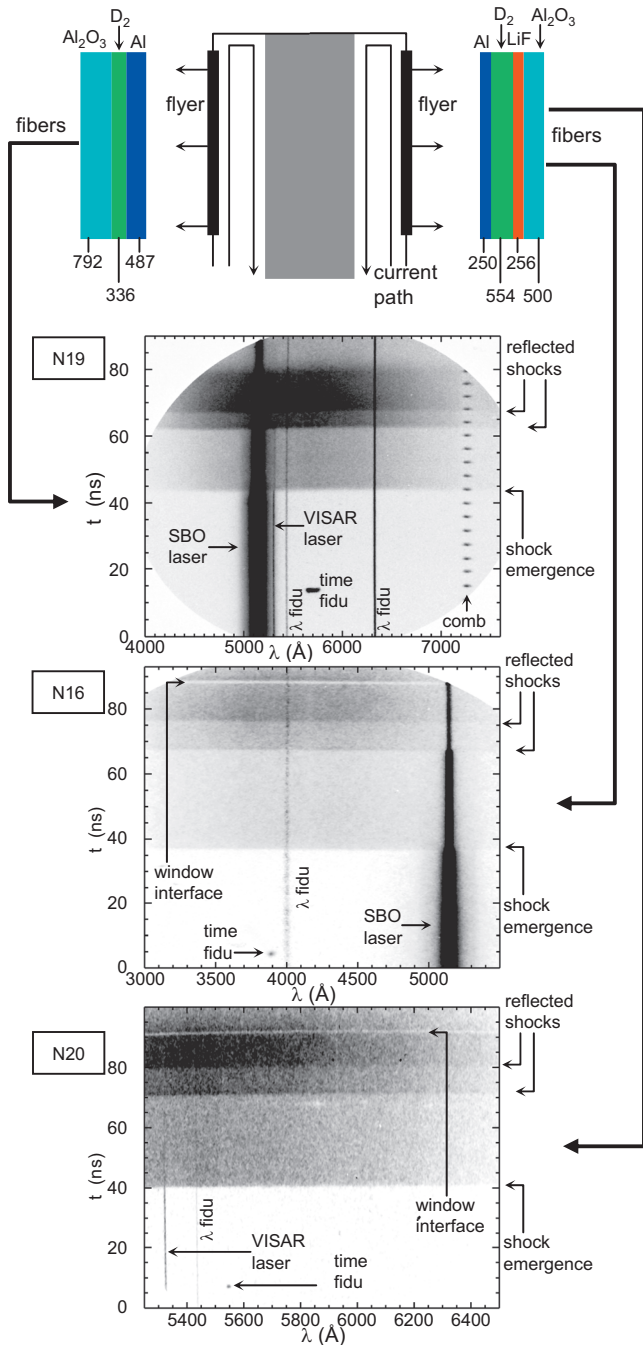


FIG. 1. (Color) Schematic diagram and typical streaked optical spectra from a dual-cell D_2 experiment (No. Z824). The cell component dimensions are indicated in microns. Light collected in optical fibers viewing the back of the D_2 cell through Al_2O_3 and/or LiF windows is injected into streaked optical spectrometers.

dence of the shocked D_2 self-emission (Fig. 2). The relationship between the spectral radiance and pressure was obtained from quantum molecular-dynamics (QMD) calculations.¹¹ These calculations use the Vienna *ab initio* simulation program⁴¹ to perform simulations for collections of 128 atoms using the generalized gradient approximation (GGA) for the density-functional theory exchange and correlation functionals. These simulations are similar to the earlier work reported in Ref. 12, but with a higher degree of convergence

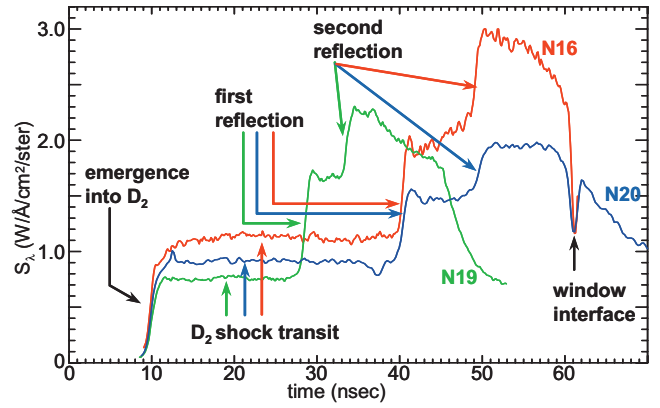


FIG. 2. (Color) Time direction lineouts from the three spectral images in Fig. 1. The lineouts are centered at 5881 Å, 4470 Å, and 5860 Å and averaged over wavelength ranges of 783 Å, 920 Å, and 557 Å for systems N19, N16, and N20, respectively. The leading edges have been time shifted to agree at the 50% level of the initial shock emergence into the D_2 cell. During the constant emission phase the spectral radiance differences between the systems arise from the difference in the lineout wavelength as well as calibration differences, measurement errors, and differences between the two D_2 cells.

on the thermodynamic quantities. Following the molecular-dynamics calculations, 10–20 configurations selected from the equilibrated portion of the time history were analyzed for their optical properties using the Kubo-Greenwood approach along the lines reported in Refs. 12 and 13. QMD calculations of the spectral radiance as a function of pressure are shown in Fig. 3 at three wavelengths spanning the range used in experiments. These *ab initio* calculations provide a self-consistent description of the shock pressure, density, temperature, and the wavelength-dependent emissivity. QMD calculations agree well with Hugoniot measurements^{11,25} and with the results presented below. Determination of pressure steadiness requires only knowledge of the *relative* spectral radiance variation with small changes in the *relative* pressure. Therefore, we expect this determination to be highly insensitive to residual model uncertainties.

The determination of relative pressure as a function of time $P(t)$ is straightforward, once we possess the relationship between S_λ and P (Fig. 3) and measurements of $S_\lambda(t)$

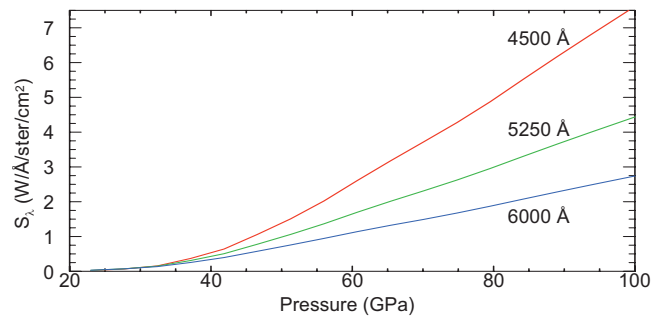


FIG. 3. (Color) Spectral radiance S_λ as a function of pressure calculated with QMD simulations (Ref. 11). S_λ includes temperature and emissivity influences on the wavelength-dependent emission.

(Fig. 2). A set of representative relative pressure vs time results is shown in Fig. 4. The rising edge of the Fig. 4 pressure history plots was shifted so that $t=0$ corresponds to 90% of the pressure during the initial shock transit through D_2 . The pressure increase at the right side of the 22.2–75.5 GPa plots corresponds to the reflection of the shock at the D_2 /window boundary. The pressure decrease at the right side of the 89 GPa plot probably corresponds to the arrival of a rarefaction wave from the thin flyer used to obtain the higher pressure. The duration of the steady pressure is longer than 30 ns at the lower pressures and it remains above ~ 10 ns at the highest pressure. The observed duration at the lower pressures is limited by the width of the D_2 cell. The pressure change during the initial shock transit across the D_2 cell was determined by averaging the pressure over a 3 ns interval at the beginning and end of the transit, subtracting the value at the beginning from the value at the end, and dividing by the beginning value. Thus, a negative value corresponds to decreasing pressure. The average of the pressure change during the D_2 shock transit over the 32 measurements was $-1.2 \pm 1.9\%$, where the uncertainty here corresponds to the standard deviation. In some experiments the change was smaller than $\sim \pm 0.3\%$. The results are presented in Table I. The inferred pressure change depends on the average rate of change in the spectral radiance, the shock transit duration, and any contributions to the spectral radiance variation that arise from measurement errors. For example, sweep rate variations or streak camera spatial sensitivity variations at the few percent level will contribute to the apparent pressure variation. Such errors would appear randomly throughout the data set since five different streak cameras were used over a three year period. The fact that roughly 1/3 of the measurements indicate increasing pressure and 2/3 of the measurements indicate decreasing pressure further indicates that measurement errors may contribute to the observed variation and the actual pressure change may be smaller than the values reported in Table I. The percent pressure change per nanosecond was estimated by fitting the pressure vs time data over the D_2 shock transit interval with a straight line. The average pressure slope was -0.14% dP/ns ($\sim 1.4\%$ over 10 ns). However, the best measurements possess less than 0.03% dP/ns slopes, reflecting a pressure change of less than 1% over a 30 ns interval. Again, these changes include any apparent pressure differences due to measurement error. Consequently, the actual pressure change rates may be lower.

IV. RESULTS: REFLECTIVITY/EMISSIVITY

Strong shocks change liquid D_2 from a transparent insulator to a conducting metal-like material with finite specular reflectivity. This feature is intrinsic to the ability to measure the shock velocity using VISAR, a key enabling technique for building EOS understanding. The finite reflectivity is important for two additional reasons. First, reflectivity measurements can test models of the insulator-conductor transformation. Second, the shock front emissivity can be inferred from the reflectivity. Emissivity knowledge is a key ingredient of temperature determination from spectral radiance measurements.

The principles of D_2 shock front reflectivity measurements were established in prior work.³⁰ Laser light injected into the D_2 cell initially reflects from the Al pusher. Measurements of the reflected intensity before and after the shock emerges into the liquid D_2 can be used to infer the D_2 shock reflectivity, provided the Al pusher reflectivity is known. The challenges of implementing this method include ensuring that the detector measuring the initial large laser signal that reflects from the Al is not saturated and that the weaker signal during the shock propagation phase is measured with adequate signal to noise. Additional potential difficulties include accurate measurements of the laser signal above the self-emission of the shocked D_2 , accounting for possible geometrical collection efficiency differences as the spatial position of the reflection changes, possible time-varying attenuation in the unshocked portion of the liquid D_2 cell as the shock moves and shrinks the unshocked portion, and stray light contributions from elsewhere in the cell, particularly for multithickness cells employed in some of the experiments described here. An antireflection coating applied to the window surfaces helps prevent undesired reflections from influencing the results. Also, the results below used a variety of experimental setups, including differences in the lateral spacing between the send fiber and the spectroscopy collection fiber, cell and window thickness, and window material. The reasonably small standard deviation of the average reflectivity/emissivity values indicates that geometrical and stray light effects did not strongly influence the results.

The streaked spectrograph measurements clearly distinguish the laser light from the self-emission (Fig. 1). On the other hand, the injected laser intensity in these experiments was optimized for the VISAR and SBO measurements and not for the streaked spectrometer detection. Consequently, in some experiments the dye laser employed for the SBO diagnostic was intense enough that the streaked spectrometer signal was saturated and in others the VISAR signal was too weak for accurate detection. These difficulties illustrate the desirability of spectrally resolved measurements: detector saturation was clearly identified as a change in the wavelength-dependent laser intensity profile between the high-reflectivity Al-reflection phase and the low-reflectivity D_2 shock propagation phase.

The reflectivity was determined by taking wavelength direction lineouts through the streaked spectra that averaged over the period just before and just after the shock emergence into the D_2 cell. Representative lineouts at shock pressures spanning the 20–75-GPa range are shown in Fig. 5. The left plot at each pressure shows the as-measured laser signals, illustrating the intensity decrease during the D_2 shock propagation phase. The signal drops more at lower pressures, indicating that the insulator-metal transformation is incomplete and consequently the reflectivity is lower. The right plot at each pressure shows the signals with the D_2 shock reflection multiplied by the indicated scale factor. The collection of plots in Fig. 5(a) represents unsaturated signals that were used for the reflectivity determination. The Fig. 5(b) plot represents an example of a saturated laser signal. It illustrates the spectral profile change that serves as a signature for saturation. Unsaturated laser spectral profile measurements [e.g., Fig. 5(a)] were fit using the ROBFIT (Ref. 42)

TABLE I. Results from initial shock transit across the D_2 cell, designated with a Z shot number (multiple D_2 cell locations are further designated with /N or /S for the North or South side of the apparatus). The spectrometer system is identified with a 16, 18, 19, 20, 21, or 22. $\langle U_s \rangle$ is the shock velocity (Ref. 25). P is the shock pressure from Ref. 25, except values with an asterisk were obtained from Ref. 25 pressure vs. $\langle U_s \rangle$ results combined with spectroscopy shock velocity measurements. dP is the total pressure change, dP/dt is the pressure change per unit time, and “ dt -steady” is the steady pressure duration. ϵ is the emissivity. T_{abs} is the absolute method temperature and T_{minabs} , T_{maxabs} are the corresponding lower and upper bounds. T_{rel} , T_{minrel} , and T_{maxrel} are similar relative method quantities.

Z####/ cell	Sys	$\langle U_s \rangle$ ($\mu\text{m}/\text{ns}$)	P (GPa)	dP (%)	dP/dt (%/ns)	dt steady (ns)	ϵ	T_{abs} (eV)	T_{minabs} (eV)	T_{maxabs} (eV)	T_{rel} (eV)	T_{minrel} (eV)	T_{maxrel} (eV)
904/N	19	13.5 ± 0.24	22.2 ± 0.6	1.8	0.051	32	0.95	0.461	0.446	0.483	0.468	0.427	0.517
904/S	20	13.61 ± 0.27	22.4 ± 0.7	0.5	0.079	33		0.435	0.419	0.456	0.408	0.352	0.488
904/N	16	13.5 ± 0.24	22.2 ± 0.6				0.86						
698	19	15.78 ± 0.15	31.4 ± 0.6	-1.2	-0.102	15	0.89	0.519	0.499	0.547	0.585	0.508	0.685
698	20	15.78 ± 0.15	31.4 ± 0.6	-1.2	-0.048	30	0.96	0.546	0.523	0.579	0.918	0.639	1.794
895/S	20	15.72 ± 0.39	31.3 ± 1.1	0.9	0.046	29	0.86	0.554	0.529	0.588	0.451	0.377	0.565
895/N	16	15.41 ± 0.39	31.0 ± 1.1				0.75						
592	18	15.99 ± 0.31	33.9 ± 1.6	-0.5	-0.054	11					0.416	0.299	0.724
592	19	15.99 ± 0.31	33.9 ± 1.6								0.600	0.525	0.696
792/S	18	17.91 ± 0.39	41.1 ± 1.1	-5.8	-0.240	26	0.86	0.703	0.667	0.752	0.944	0.635	2.355
792/N	19	17.98 ± 0.40	41.7 ± 1.1	-0.7	-0.075	14	0.83/0.86	0.622	0.595	0.661	0.720	0.617	0.869
792/S	20	17.91 ± 0.39	41.1 ± 1.1	-2.2	-0.276	12					0.637	0.495	0.923
792/N	16	17.98 ± 0.40	41.7 ± 1.1				0.92						
824/N	19	18.02 ± 0.10	42.1 ± 1.0	0.1	0.016	15	0.83	0.730	0.692	0.783	0.769	0.658	0.924
824/S	20	17.97 ± 0.11	42.6 ± 1.0	-0.6	-0.038	22		0.775	0.730	0.838	1.238	0.756	5.886
824/S	16	17.97 ± 0.11	45.6 ± 1.0	1.9	0.0074	27	0.80				0.553	0.490	0.636
1108/N	19	18.34 ± 0.10	42.4 ± 1.2	-1.4	-0.048	27	0.90	0.873	0.840	0.913	0.724	0.625	0.865
593	19	18.63 ± 0.15	45.2 ± 2.0	0.9	0.0069	25					1.040	0.827	1.437
762/N	16		42.7^*	-2.3	-0.119	24					0.796	0.701	0.922
632	16		43.0^*								0.543	0.457	0.663
632	19		39.0^*								0.798	0.669	0.992
761/S	19		63.4^*	-2.2	-0.248	12		1.207	1.114	1.338	1.158	0.887	1.753
761/S	20		63.4^*	-6.3	-0.789	11		1.422	1.296	1.606	1.210	0.761	4.258
634	18	22.48 ± 0.19	65.3 ± 1.2	-1.9	-0.285	10		1.462	1.290	1.757	1.694	0.694	
634	19	22.48 ± 0.19	65.3 ± 1.2	1.0	0.071	20					1.091	0.872	1.478
710	19	23.25 ± 0.19	69.7 ± 1.3	0.1	0.018	8	0.65	1.122	1.041	1.237	1.188	0.922	1.698
710	16	23.25 ± 0.19	69.7 ± 1.3								1.010	0.843	1.269
710	18	23.25 ± 0.19	69.7 ± 1.3	-1.4	-0.220	9					1.660	0.946	
1109/S	21	23.30 ± 0.36	70.2 ± 1.9	-1.2	-0.080	18	0.73	1.291	1.227	1.370	1.335	0.688	
1109/N	22	23.43 ± 0.38	70.9 ± 2.0				0.68						
711	19	23.23 ± 0.19	70.5 ± 1.6	0.4	0.077	10	0.62	1.175	1.087	1.301	1.120	0.877	1.576
711	18	23.23 ± 0.19	70.5 ± 1.6	-2.7	-0.16	23		1.112	1.036	1.219			
791/N	16	23.57 ± 0.50	70.7 ± 2.3	-0.4	-0.047	10					0.988	0.8215	1.256
791/N	19	23.57 ± 0.50	70.7 ± 2.3	-2.5	-0.214	19		1.733	1.569	1.972	3.609	2.024	
791/S	18	23.49 ± 0.41	70.5 ± 2.1	-2.6	-1.21	5		1.923	1.737	2.191	1.129	0.697	5.790
791/S	20	23.49 ± 0.41	70.5 ± 2.1	-3.3	-0.284	16		2.275	2.027	2.642			
894/N	16	24.10 ± 0.22	75.5 ± 1.7				0.71				1.089	0.876	1.471
894/N	19	24.10 ± 0.22	75.5 ± 1.7	-0.2	-0.02	17		1.619	1.472	1.829	1.685	1.162	3.343
1111/N	19	24.94 ± 0.44	81.3 ± 2.2	0.5	0.021	14	0.66	1.470	1.365	1.609			
1111/N	22	24.94 ± 0.44	81.3 ± 2.2				0.80						
1110/N	19	26.11 ± 0.47	89.3 ± 2.4	-2.3	-0.193	14		1.771	1.619	1.984			
1110/S	21	26.44 ± 0.50	90.3 ± 2.4	-2.3	-0.164	17		2.105	1.899	2.400			

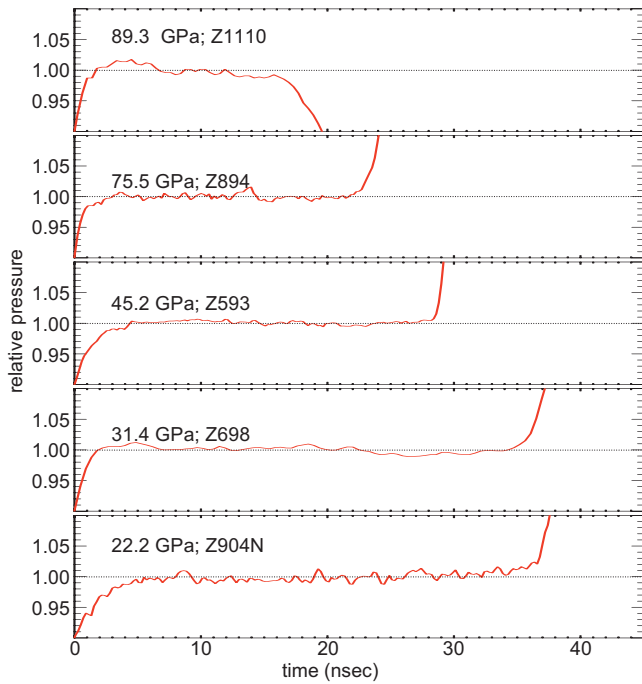


FIG. 4. (Color) Relative pressure as a function of time measured in representative experiments spanning the range of pressures reached in the singly shocked D_2 .

spectral line fitting code. This objectively determines both the most probable intensity value and the typically $\sim \pm 5\text{--}10\%$ intensity uncertainty that arises from noise. The reflectivity during the D_2 shock propagation phase was then determined from $R_{D_2} = R_{Al} / (I_{Al} / I_{D_2})$, where R_{Al} is the initial Al reflectivity and I_{Al} and I_{D_2} are the intensities from the Al-reflection and D_2 reflection periods, respectively. Measurements of R_{Al} were not performed for the actual Al pushers used in these experiments. Instead, calibrations were performed to measure the reflectivity of an Al sample prepared using the same diamond-turning fabrication technique as the actual cell components. We found that $R_{Al} = 0.80$ over the $0\text{--}12^\circ$ reflection angles sampled by the fiber collection system employed here.

The shocked D_2 emissivity (ε) was inferred from the reflectivity measurements assuming $\varepsilon = 1 - R$. The individual emissivity results are presented in Table I and the average emissivity as a function of pressure is shown in Fig. 6. Note that some experiments provide only an emissivity measurement because high-quality laser signals can be obtained even if the streak camera sensitivity is set too low to accurately record the self-emission. The emissivity as a function of pressure agrees reasonably well (Fig. 6) with the predictions of the QMD calculations described above. The normalized $\chi^2 = 2.1$, reasonably close to unity considering the complexity of the experiments and calculations. The QMD calculations¹¹ provide the wavelength-dependent emissivity (Fig. 7), an important capability for the determination of temperature described below. The emissivity measurements are a compilation of results using the VISAR (5320 Å) and dye (5140 Å) lasers and the QMD calculations shown in Fig. 6 correspond to 5250 Å. At each pressure group we have averaged the available emissivity measurements and the error bars shown

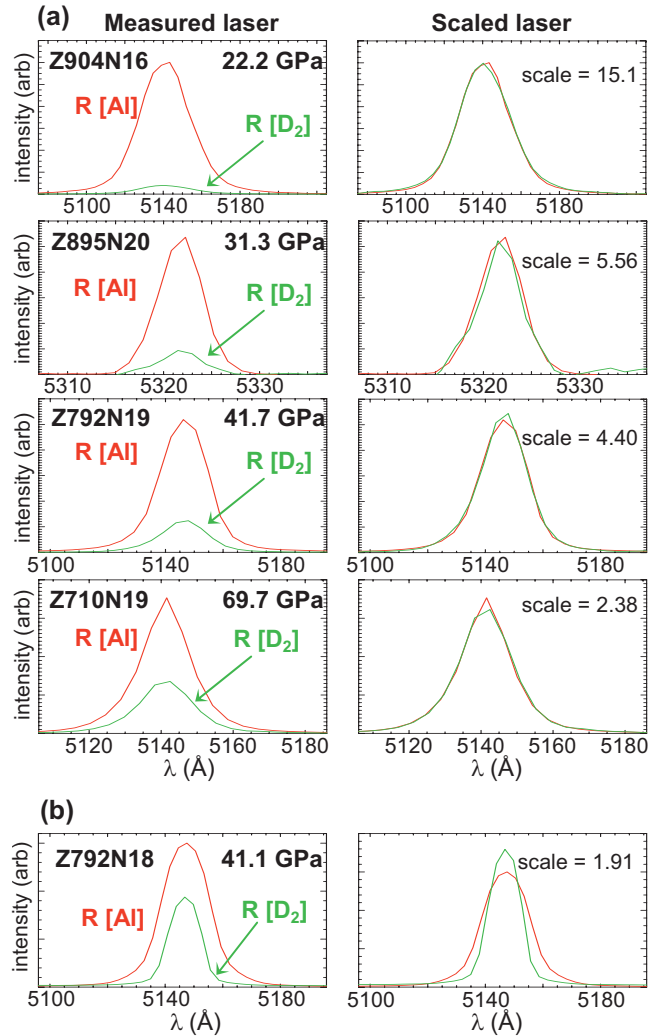


FIG. 5. (Color) Lineouts measuring the reflected laser intensity profile on representative experiments. $R[Al]$ is taken during the period when the light reflects from the rear Al pusher surface, before the shock emerges into the D_2 . $R[D_2]$ corresponds to reflection from the shock front during the first transit through the D_2 cell. Plots at the left show the as-measured signals, illustrating the reduced reflection from the D_2 shock front, in comparison to the Al pusher. Plots at the right show the signals with the $R[D_2]$ lineout amplitude scaled up by the indicated amounts. The plots in (a) represent experiments with good quality unsaturated laser signals. The shape agreement confirms that the signals are free of saturation effects, while the amplitude scale factor provides a measure of the D_2 shock front reflectivity. The plots in (b) represent a measurement with a saturated laser signal.

in Fig. 6 correspond to the 1σ standard deviation. The average standard deviation is $\sim \pm 8\%$. The QMD calculations fall within the 1σ error bars at three of the four pressures. The difference at 40 GPa is beyond the 1σ error bar, indicating that further measurements should be performed to evaluate whether this difference arises from measurement errors or if a refinement in the QMD model is needed. The Fig. 6 emissivity results agree with the measurements reported in Ref. 30 at the 22-GPa and 70-GPa pressure values, within the combined uncertainties. The agreement at 70 GPa is significant because it represents the regime where the reflectivity

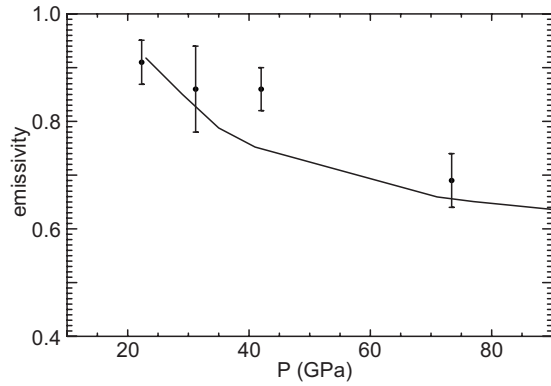


FIG. 6. Comparisons of measured emissivity (dots with error bars) with QMD calculations (solid line). The dots represent averages over 2, 4, 7, and 7 measurements at 22, 32, 42, and 74 GPa, respectively. The error bars correspond to the 1σ standard deviation. The measurements were performed at either 5320 Å or 5140 Å, while the calculations correspond to 5250 Å.

ity has saturated at its metal-like value. However, the present emissivities from both the measurements and the QMD calculations are higher than Ref. 30 at 30–40 GPa. This regime is important since it is where the insulator-conductor transformation occurs. Further experiments specifically dedicated to higher accuracy reflectivity measurements are needed to resolve this difference.

V. RESULTS: TEMPERATURE

The shocked D_2 temperature was inferred from measurements of the wavelength-dependent spectral radiance combined with knowledge of the emissivity, under the approximation that the shock self-emission may be represented as a Planck spectrum modified by ϵ_λ . Planckian spectra multiplied by the QMD emissivity were fit to the measured spectral radiance. The normalized χ^2 averaged over all the experiments was $\chi^2=1.6$, confirming that the assumed Planckian spectral shape is a valid representation of the data. The analysis methods were described in Ref. 33. Two separate approaches, designated the *absolute* and *relative* methods, were employed. In many experiments a calibration provided the absolute spectral radiance as a function of wavelength. In these cases we infer the temperature using the *absolute* method³³ to fit the measured spectrum while simul-

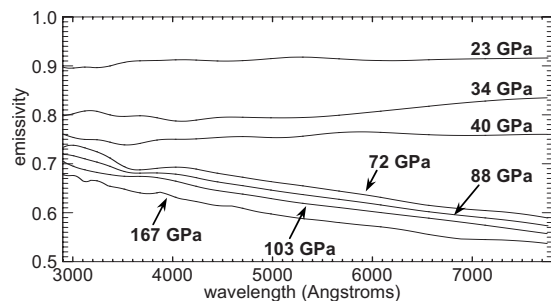


FIG. 7. Shocked D_2 emissivity vs wavelength at pressures spanning 23–167 GPa, calculated with QMD simulations (Ref. 11).

taneously accounting for the absolute spectral radiance, wavelength dependence, and absolute emissivity as a function of wavelength $\epsilon(\lambda)$. In the *relative* method the temperature was inferred by fitting the relative spectrum intensity as a function of wavelength, without regard for the absolute intensity. In this case we employ QMD calculations of $\epsilon(\lambda)$, but only the relative emissivity change as a function of wavelength is important. The relative method has the advantages that relative calibrations are more accurate than absolute calibrations and it avoids uncertainty contributions from the absolute emissivity value. However, the spectrum shape changes corresponding to small temperature changes are not as readily measured as absolute intensity changes. In particular, relative changes in the 3000–7000-Å range examined here become too small to measure for temperatures above approximately 1 eV, since this spectral regime corresponds to the red wing of the spectrum³³ and the spectral shape of the red wing changes more slowly as the temperature is increased. The absolute method has the advantage that relatively large changes in the spectrum arise from small temperature changes and the method can be applied at all temperatures reached in these experiments. The challenges of the absolute method include the difficulty of absolute calibrations and additional influence of emissivity uncertainties.

Example fits to the spectral radiance are shown in Figs. 8(a) and 8(b) for the absolute and relative methods, respectively. The relative system sensitivity as a function of wavelength was measured prior to each experiment, including the fiber optics, spectrograph, and streak camera detector. The uncertainty in the relative sensitivity is assigned to be the standard deviation of all the calibrations performed over the three year period of these experiments. This estimate is very conservative since it includes the combination of the actual calibration uncertainty plus whatever real variation in the relative efficiency occurred over the campaign. The absolute sensitivity was also measured for most of the spectrometer systems prior to each experiment. The absolute uncertainty accounts for the uncertainty in the fiber connection throughput ($\pm 3\%$), the $\pm 2\%$ sweep rate drift during the 4–24 h time between performing the calibration and the actual Z experiment, the measured total system efficiency (typically $\pm 14\%$), and emissivity ($\pm 16\%$) (see Ref. 33). The results reported here used the emissivity $\epsilon(\lambda)$ calculated by the QMD simulations, shown above to be in generally good agreement with the $\epsilon(5140 \text{ Å})$ and $\epsilon(5320 \text{ Å})$ measurements. The emissivity values were conservatively assigned to have an uncertainty of $\pm 16\%$ for the purpose of computing the contribution of the emissivity uncertainty to the temperature uncertainty. This is twice the 1σ standard deviation actually determined in the emissivity measurements described above. In order to investigate the sensitivity of the inferred temperature to the emissivity we also computed temperatures using the absolute method with wavelength-independent emissivities set equal to the values reported in Refs. 29 and 30. The temperature using this emissivity approximation was higher than the values reported below by an average of 5%. In Fig. 8 the solid lines correspond to the optimum temperature value and the dashed lines represent the temperature corresponding to the 1σ bounds. The dotted line represents the increased uncertainty ($\pm 1.8\sigma$) needed to bring the abso-

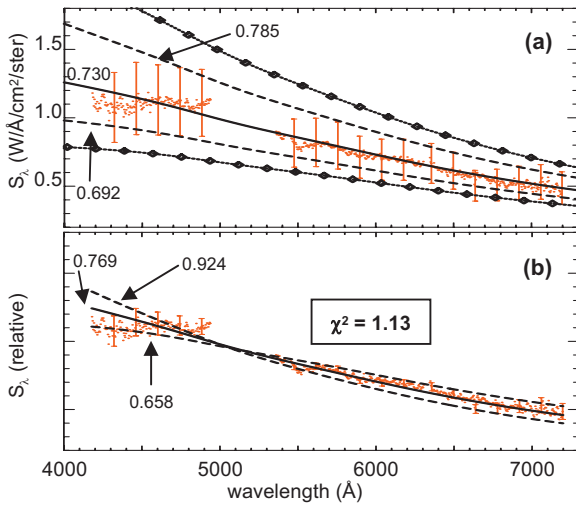


FIG. 8. (Color) Fits to measured spectral radiance used to infer the shocked D_2 temperature in experiment No. Z824 N19 (see Figs. 1 and 2). The absolute method fit is shown in (a) and the relative method fit is shown in (b). The red dots are the measurements. Each spectrum consists of approximately 300 wavelength channels, but the 1σ uncertainties are shown for a reduced number of points for clarity. The gap in the data between 4900–5400 Å is due to the strong SBO and VISAR laser signals that interfere with the self-emission measurements (Fig. 1). The solid line is the fit representing the most probable temperature value and the dashed lines represent the $\pm 1\sigma$ temperature values. The temperature values corresponding to each fit are given in electron volts. The normalized χ^2 for the best fit is given in (b), indicating good agreement between the Planckian spectrum multiplied by the emissivity and the data. The dotted curves on the absolute method plot correspond to $\pm 1.8\sigma$ temperature values (see text).

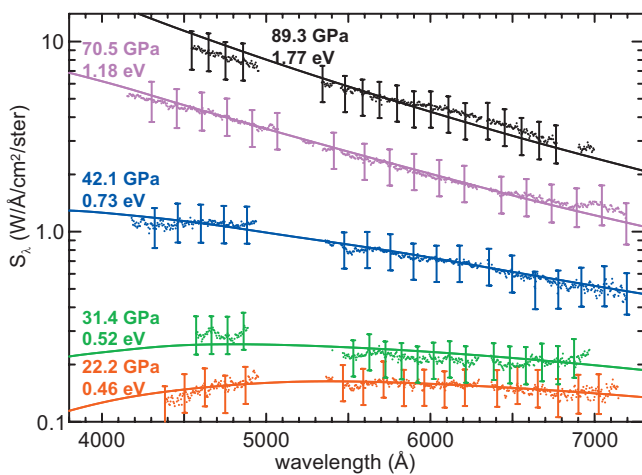


FIG. 9. (Color) Fits (solid lines) to representative S_λ measurements (dots; a reduced subset of the data are shown with error bars) spanning the shocked D_2 pressures reached in these experiments. The fits were performed using the absolute method and the most probable temperature is indicated with each fit, accompanied by the experiment pressure. The data correspond to experiment Nos. Z904N19, Z698N19, Z824N19, Z711N19, and Z1110N19 at the 22.2, 31.4, 42.1, 70.5, and 89.3 GPa pressures, respectively (see Table I).

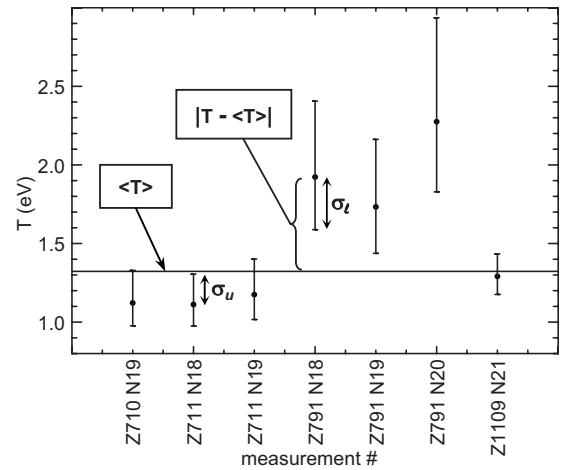


FIG. 10. Collection of absolute method temperature measurements obtained at 70.3 GPa. The error bars correspond to $1.8\times$ the nominal 1σ uncertainties. The weighted mean $\langle T \rangle$ is shown as a solid line. The upper bound uncertainties σ_u are larger than the lower bound σ_l . The deviation of each measurement away from the weighted mean is $|T - \langle T \rangle|$ and the dimensionless deviation is either $D = |T - \langle T \rangle| / \sigma_u$ or $D = |T - \langle T \rangle| / \sigma_l$, depending on whether the measurement is below or above the weighted mean, respectively.

lute method measurement distribution into agreement with a Gaussian distribution, as described below. A set of representative spectral radiance fits using the absolute method at five different pressures is shown in Fig. 9. As the shocked D_2 pressure increases the spectral radiance absolute intensity increases and the spectral shape changes. The resulting changes in the inferred temperature are indicated in Fig. 9. Both Figs. 8 and 9 illustrate the good agreement between the

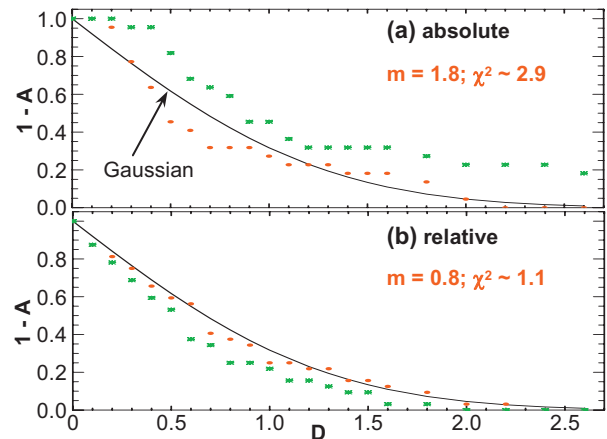


FIG. 11. (Color) Probability $1-A$ that a measurement will be more than $D\sigma$ away from the mean, plotted as a function of D , where D is the dimensionless deviation and A is the area under the distribution within the bounds $\pm D\sigma$. The solid line represents the expectation for a Gaussian distribution (for example, at $D = 1.0$, 31.7% of measurements are expected outside the $\pm D\sigma$ bounds). The green points are the experiment distributions with the nominal uncertainty estimates for the absolute (a) and relative (b) methods. The red points correspond to adjustments in the temperature uncertainties by 1.8 and 0.8 for the absolute and relative methods, respectively.

measured spectral radiance wavelength dependence and Planckian spectra multiplied by the emissivity.

Each individual temperature measurement provides an estimate T_i for the true value of the shocked deuterium temperature. The collection of individual measurements can be used to determine which models are consistent with the data set and which are not. The ability to constrain models depends on the temperature uncertainties that range from ± 3 –12%. The model tests can be made more severe by grouping the results in small pressure intervals and constructing a weighted mean, $\langle T \rangle = \sum(T_i / \sigma_i^2) / \sum(1 / \sigma_i^2)$, that is a more accurate estimate for the true temperature. Here, σ_i is the uncertainty in the i^{th} individual temperature measurement T_i . An example data set corresponding to the absolute method results at 70.3 GPa is shown in Fig. 10. This weighted averaging requires the assumption that the data are distributed according to Gaussian statistics. The large collection of data assembled over the three-year period of these experiments enabled us to evaluate the validity of this assumption. To the best of our knowledge, such an evaluation has not been previously performed in shock physics experiments.

A meaningful comparison of the measurement distribution with Gaussian statistics requires a large number of measurements, but the number of measurements at any single pressure group is insufficient. We overcome this difficulty by exploiting the concept of dimensionless deviation $D = |(T_i - \langle T \rangle) / \sigma_i|$ (Ref. 43, pg. 252; see Fig. 10). The fraction of measurements $f(D)$ that are more than $D\sigma$ away from the mean value is $1 - A$, where A is the integral under the Gaussian distribution over the range $\pm D\sigma$ (Fig. 11, solid line). Expressing the deviation of the measurement away from the mean as a fraction of the 1σ uncertainty enables us to examine the distribution of all the measurements in a single group.

There is an additional complication that must be overcome: the temperature uncertainties are not symmetric. The temperature measurements are based on fitting the spectral radiance measurements with calculated spectra corresponding to different Planckian temperatures and computing χ^2 . As the temperature is varied away from the best fit value, χ^2 grows faster for variations that are below the best fit value than for variations above the best fit value. This results from the fact that the optical spectrometers measure the spectral radiance on the long wavelength side of the Planck spectrum maximum. Thus, the uncertainties above each data point are larger than the uncertainties below each data point (see Fig. 10).

We address this problem by assuming that the data points below the true value and above the true value are both distributed according to Gaussian probability distributions with the same mean, but with widths that are different. This treatment is suggested by Bevington and Robinson (Ref. 43, p. 211). The weights for data values below the mean are therefore the upper uncertainties and the weights for data values above the weighted mean are the lower uncertainties. The uncertainty in the weighted mean is asymmetric (as are the individual uncertainties that underlay the analysis), with upper bound $\sigma_u = 1 / \sum(1 / \sigma_{ui}^2)$ and lower bound $\sigma_l = 1 / \sum(1 / \sigma_{li}^2)$, where the sum runs over all data points. These assumptions are supported by the fact that the *relative* and *absolute* analy-

sis methods yield results that agree to within the uncertainties, even though the asymmetry resulting from the two methods is different.

The results of comparing the experimental temperature distributions with the expectation for a Gaussian are shown in Figs. 11(a) and 11(b) for the *absolute* and *relative* methods, respectively. The two methods are treated separately since the phenomena that might influence the results are different. Both methods possess a distribution shape that is in very reasonable agreement with Gaussian statistics. However, to obtain agreement for the width of the absolute method distribution it is necessary to multiply the uncertainties by a factor of 1.8. The fraction of measurements that are more than $D\sigma$ away from the mean for the nominal uncertainties is shown with green asterisk symbols. The result for uncertainties increased by a factor of 1.8 is shown with red dots. This implies that undetermined processes altered the measurements and introduced measurement scatter beyond the estimated uncertainties. For example, when the D_2 cell is cooled it is possible that residual gas condenses on the exit window and attenuates the signal. Alternatively, stray light could enter the cell from the plasmas that are ubiquitous in creating the high energy density conditions in these experiments. Both of these possible mechanisms would be considered systematic effects in a single experiment, but contribute randomly to the large collection of experiments conducted over several years. The importance of compiling a large enough data set to enable a quantitative evaluation of the statistics is now apparent: this evaluation provides the ability to include effects that contribute to the uncertainty but are difficult to monitor by the usual consideration of the apparatus.

The evaluation of the relative method distribution indicates that the relative uncertainties are slightly too large. As in the absolute method results, the result of the nominal uncertainties is shown with green asterisk symbols and the result of decreasing the uncertainties by a factor of 0.8 is shown as red dots. This implies that the unknown mechanisms contributing to the variation in the absolute method temperatures did not affect the relative method results, most likely because the mechanisms altered the absolute light intensity without changing the wavelength dependence. Instead, the conservative approach we adopted to estimate the relative uncertainties evidently led to overestimates.

The collection of thirty-seven individual temperature measurements is presented in Table I. A compilation is shown as a function of shocked D_2 pressure in Fig. 12(a), including all the absolute method results, while the relative method results are only included on those experiments where no absolute measurement was available. This choice was dictated by the fact that the absolute method provides greater accuracy, even after multiplying the uncertainties by 1.8. In addition, the relative method reliability suffers for temperatures above approximately 1 eV, potentially affecting results at D_2 pressures above about 60–70 GPa. The weighted average temperature values in the seven pressure groups indicated in Table I are listed in Table II and plotted as a function of pressure in Fig. 12(b). The uncertainties in both Table II and Fig. 12 correspond to the factor of 1.8 increase in the absolute method results and the factor of 0.8 decrease in the

relative method results. The Table I uncertainties are the original nominal values.

It is useful to compare the absolute and relative method results since the methods have different advantages and disadvantages and the phenomena that could systematically bias the results are different. An examination of Table I shows that only two of the eighteen measurements with results from both methods are different by more than the nominal 1σ uncertainties. Furthermore, the absolute and relative weighted means agree to within the uncertainties for all five pressure groups where data from both methods exist (Table II). Therefore, no statistically significant difference exists between the results from the two methods. This provides evidence that the absolute emissivity uncertainties have not biased the absolute method temperature results.

The weighted mean temperatures from the combined data set (absolute results where available, relative where no absolute is available) are also shown in Table II. Combining results from the two methods reduces the uncertainties, since more measurements are incorporated into the average. The uncertainty in the 42.1-GPa pressure group that has the most

measurements is $\sigma_u \sim +4.0\%$, $\sigma_l \sim -2.9\%$. The weighted mean from this combined data set should provide the best model constraints since the uncertainties are the smallest.

Prior temperature measurements of singly shocked liquid deuterium have been performed with both gas gun and laser facilities. Gas gun driven shock temperatures were reported¹⁸ for 11.3–23.4-GPa pressures. Laser-driven shock temperatures were reported²⁹ in the 31–230-GPa pressure range. These measurements used five or six pyrometer channels to measure the spectral radiance with $\pm 10\%$ and $\pm 30\%$ uncertainty in the gas gun and laser driven experiments, respectively. The gas gun experiments used two parameter fits to the shape and intensity of the measured spectral radiance to infer the emissivity and the temperature, with an estimated temperature uncertainty of $\pm 5\%$. The laser-driven experiments used a Drude model combined with reflectivity measurements at 4000 and 8000 Å to specify the emissivity. The temperature was inferred from fits to the spectral radiance, with a nominal temperature uncertainty of $\pm 14\%$ over the pressure range studied here.

TABLE II. Weighted mean temperatures in seven pressure groups. The first two columns are the results obtained separately with the absolute and relative measurements. The Combined T column uses absolute method data where available and relative method data for the other measurements. The global weighted mean incorporates gas gun data (Ref. 18) and laser data (Ref. 29) from the pressures that overlap the Z data pressure groups. All uncertainties are reported at 1σ , with the individual values multiplied by 1.8 for the absolute method and 0.8 for the relative method (see text). The gas gun and laser data uncertainties were also multiplied by 1.8, to provide an equitable weighting for all results.

Pressure (GPa)	Absolute T (eV)	Relative T (eV)	Combined T (eV)	Global T (eV)	
22.3	0.453	+0.028	+0.033	+0.028	+0.019
		-0.019	-0.026	-0.019	-0.015
32.4	0.541	+0.032	+0.046	+0.030	+0.028
		-0.023	-0.032	-0.021	-0.021
42.1	0.755	+0.038	+0.037	+0.029	+0.027
		-0.028	-0.026	-0.021	-0.020
64.4	1.350	+0.018	+0.26	+0.16	+0.16
		-0.12	-0.13	-0.10	-0.10
70.3	1.323	+0.087	+0.13	+0.075	-0.073
		-0.064	-0.075	-0.053	-0.052
75.5			+0.30	+0.24	+0.23
			-0.16	-0.14	-0.14
89.8	1.944			+0.31	+0.203
				-0.22	-0.171

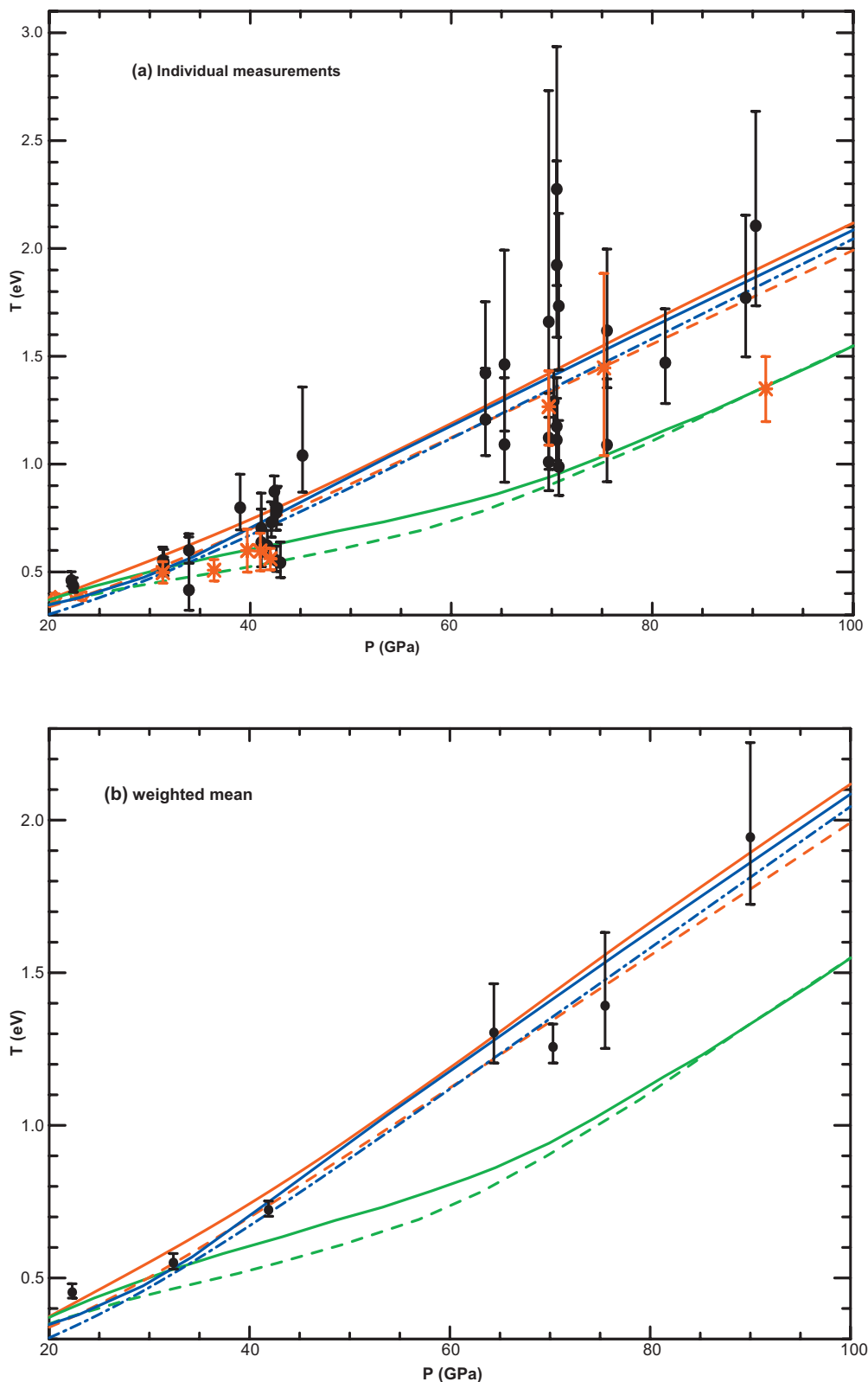


FIG. 12. (Color) Shocked D_2 temperature as a function of pressure. The thirty-seven individual measurements from Z experiments are shown as black dots with error bars in (a). The results from gas gun driven (Ref. 18) and laser-driven (Ref. 29) shock experiments are shown as red diamonds and red asterisk symbols, respectively. The weighted mean temperature values in seven pressure groups are shown as black dots in (b). The displayed 1σ uncertainties have been adjusted so that they represent the observed data distribution. The data are compared with theoretical results published by Desjarlais QMD (Ref. 11) (blue solid line), Kerley (Ref. 5) (red solid line), Lenosky *et al.* [tight-binding QMD (Ref. 7)] (red dashed line), Collins *et al.* QMD (Ref. 12) (blue dot-dash line), Ross (Ref. 4) (green solid line), and Young (Ref. 6) (green dashed line).

The gas gun and laser experiments cannot be directly compared, since they did not report results in the same pressure range. However, both experiments can be compared with the present results. The streaked spectrometers measure the spectral radiance in approximately 300 wavelength channels with an absolute accuracy of $\pm 5\text{--}20\%$. The relative accuracy as a function of wavelength was $\pm 3\text{--}10\%$. The temperature uncertainties in the present experiment were initially estimated from the calibrations, considerations of the apparatus, and the fit accuracy. The absolute method provides uncertainties that are often as low as $\pm 5\%$. The combined data set consisting of absolute method results where available and relative method results elsewhere has an uncertainty averaged over all the experiments of -11% and $+18\%$ for the lower and upper limits, respectively. These values increase to -13% and $+21\%$ after adjusting the uncertainties so that they represent the observed scatter in the data. Thus, the uncertainties in the present experiments are comparable to the prior work. However, there are three aspects that increase the significance of the present measurements:

(1) The large number of measurements enables the quantitative inclusion of systematic influences that vary between experiments. Such influences are likely to exist in every temperature measurement based on spectral radiance diagnostics. To the best of our knowledge, the consideration of the data distribution is the only avenue to account for such effects. This approach requires a large number of measurements and thus was not feasible in the prior work.

(2) Utilization of streaked spectrometers provides a large number of wavelength channels that enable temperature determination from the shape of the spectrum alone, without necessity of an absolute calibration. This provides alternative

measurements that indicate no further systematic biases exist.

(3) The quantitative evaluation of pressure steadiness as a function of time ensures that pressure variations do not alter the results.

The results from the gas gun and laser experiments are included in Fig. 12(a) as red diamonds and red asterisk symbols, respectively. Some of the Ref. 29 results were reported with 1σ uncertainties and others were reported with 2σ uncertainties. To the best of our knowledge a detailed description of the origin for the Ref. 29 uncertainties has not been published and we therefore divided the 2σ error bars by two in order to obtain a consistent set of 1σ uncertainties for comparison purposes. A visual inspection shows that the results from all three techniques are in relatively good overall agreement. The gas gun driven¹⁸ shock temperatures at 22.6 and 23.4 GPa were 0.40 and 0.39 eV, respectively. Two measurements at similar pressures are available in the present experiments (Table I). The gas gun results agree with the Z904N20 datum (0.44 eV) to within the combined 1σ uncertainties. The Z904N19 datum (0.46 eV) is higher and it differs from the gas gun result by 1.3σ . We consider this to be good agreement, considering the complete independence of the approaches followed. There are eight laser-driven measurements in the pressure range studied here. The results appear to lie within the envelope of the data distribution from the present experiments [Fig. 12(a)]. Seven out of the eight Ref. 29 measurements agree with the weighted mean temperatures reported here to within 2σ . Again, this is considered to be reasonable quantitative agreement.

In a further effort to obtain unbiased results, we computed a weighted “global” mean temperature in each pressure

TABLE III. Goodness of fit evaluated for eleven different EOS models. The first column is the normalized χ^2 using the thirty-seven individual measurements. The second column is the χ^2 obtained with the smaller uncertainties associated with the combined data set weighted mean temperature. The third column also uses the combined T data but it ignores the 22.3-GPa result, motivated by the fact that this single measurement is responsible for most of the discrepancy obtained with the Desjarlais QMD (Ref. 11), Collins *et al.* QMD (Ref. 12), TB-QMD (Ref. 7), and Sesame- p (Ref. 14) models. The fourth and fifth columns are similar, but with the use of the global weighted mean obtained from a compilation of data from Z , gas gun (Ref. 18), and laser (Ref. 29) data.

Model	χ^2 individual measurements	χ^2 weighted mean	χ^2 weighted mean w/o 22.3 GPa	χ^2 global mean	χ^2 global mean w/o 22.3 GPa
Desjarlais	1.9	3.4	1.2	3.3	1.5
Kerley	1.7	2.2	2.0	2.8	3.1
GGA	2.3	6.0	1.12	6.0	0.9
TB	1.8	2.9	0.5	2.6	0.7
Ross	3.2	14.0	15.3	12.3	13.9
Young	5.3	27.2	28.9	25.2	27.1
SCVH	1.8	2.8	2.7	3.2	3.6
Sesame- p	1.6	2.0	1.3	2.0	1.9
LM-A, B	2.9	11.7	12.2	10.0	10.9
LM-H4	1.6	3.0	2.3	2.2	2.0
LM-SOCP	2.1	3.9	3.6	4.8	5.2

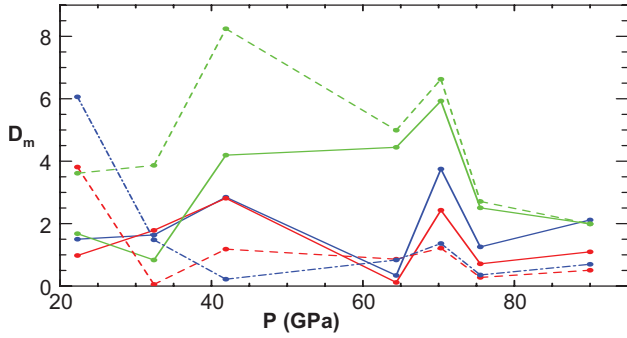


FIG. 13. (Color) Dimensionless deviation for the calculated shocked D_2 temperature compared with the weighted mean temperature measurements, as a function of pressure. $D_m = |T_m - \langle T \rangle| / \sigma_u$ or $D_m = |T_m - \langle T \rangle| / \sigma_l$, depending on whether the model is above or below the weighted mean. The color coding for the models is the same as in Fig. 12.

group using the combination of the gas gun, laser, and magnetically driven experiments. The uncertainties for gas gun and laser experiments were multiplied by a factor of 1.8 prior to constructing the mean. This represents the same adjustment for unknown systematic effects that vary from one experiment to another as employed here for the absolute method results. This amounts to assuming that the variations due to unknown effects were similar and it avoids weighting

the prior data more highly, simply because the prior data set was too small to provide an evaluation of the systematic errors. The resulting global mean temperatures are shown in Table II. The influence of including the other experiments on the weighted mean temperature results is modest. The percent change from the Z-only weighted mean temperature is -5.3% , -0.7% , -2.4% , 0% , $+0.2\%$, and -14.0% in the 22.3, 32.4, 42.1, 70.3, 75.5, and 89.8-GPa pressure groups.

VI. DISCUSSION

The results above confirm that the pressure obtained in the magnetically driven flyer plate experiments was steady. The temperature results can therefore be used to test various models for the D_2 equation of state (EOS). Predictions for shocked D_2 temperature as a function of pressure from six different EOS models are superimposed on the data in Fig. 12. This comparison includes four relatively “stiff” models^{5,7,11,12} and two relatively “soft” models^{4,6} that predict higher compressibility. It is obvious from Fig. 12 that the stiff models fit the data better than the soft models. We quantitatively evaluated the goodness of fit using the normalized $\chi^2 = \{1 / (N - m)\} \sum \{1 / \sigma_i^2 [T_i - T_m(P_i)]^2\}$, where N is the number of measurements, m is the number of free fit parameters, σ_i is the uncertainty in the i^{th} temperature measurement T_i , and $T_m(P_i)$ is the model temperature at pressure P_i . The nor-

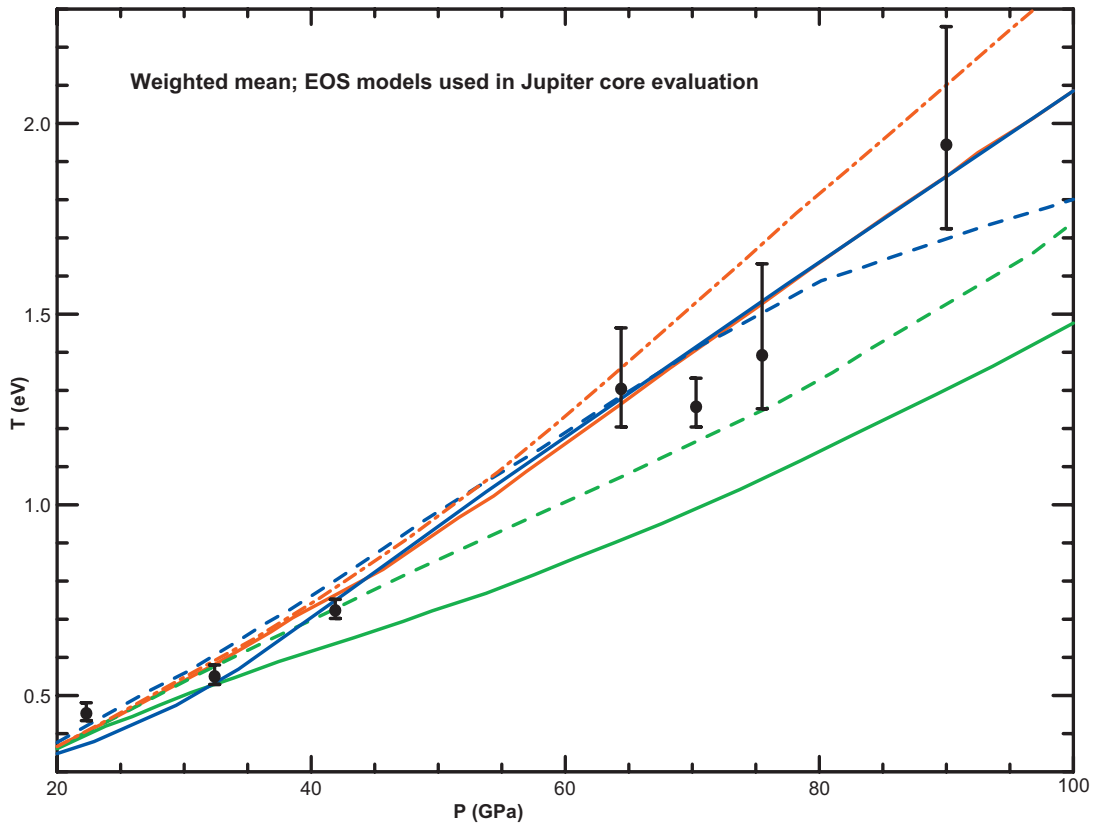


FIG. 14. (Color) Comparison of shocked D_2 temperature as a function of pressure with EOS models used to evaluate the internal structure of Jupiter (Ref. 14). The weighted mean temperature results are shown as dots with 1σ errors bars. The models employed in Ref. 14 are SCVH (blue dash), Sesame- p (red line), LM-A, B (green line), LM-H4 (green dash), and LM-SOCP (red dot dash). The QMD results from the model in Ref. 11 are shown as a blue line for comparison with Fig. 12.

malized χ^2 approaches unity for a fit that represents the data set within the 1σ uncertainties. The results (Table III) for the individual measurements range from 1.7–2.3 for the stiffer models to 3.2–5.3 for the softer models. The results from the weighted mean temperatures display the same trend: the stiff models χ^2 is significantly smaller than the soft models. The χ^2 obtained using the weighted mean is larger than from the individual results because the uncertainties are smaller. We note that even for the stiff models the weighted mean χ^2 values are greater than 2, indicating that statistically significant differences exist between the measurements and the models. In order to examine the origin of this difference we plot the dimensionless deviation as a function of pressure for the six models in Fig. 13. The color coding of the curves is the same as in Fig. 12. These results indicate that the largest contribution to the χ^2 for the stiff models arises from the 22.3-GPa measurements. In contrast, the contributions to the soft model χ^2 are large at all pressures. The third column in Table III gives the χ^2 calculated excluding the 22.3-GPa value. The normalized χ^2 is now approximately 1 for the Desjarlais quantum molecular dynamics (QMD),¹¹ Collins *et al.* QMD,¹² and tight-binding QMD⁷ results, demonstrating good agreement over the 32–90-GPa pressure range. The χ^2 values for the stiff models remain greater than ten. According to Ref. 43, the probability of χ^2 exceeding four is roughly 0.1%. Considering the conservative approach we have adopted to validate the temperature uncertainties, we must conclude that the soft models constructed in Refs. 4 and 6 do not correctly reproduce the D_2 EOS.

The χ^2 computed using the global weighted mean temperatures are also shown in Table III. The conclusions remain the same: the stiff models lead to the lowest χ^2 values and the softer models are precluded. Again the Desjarlais QMD,¹¹ Collins *et al.* QMD,¹² and tight-binding QMD⁷ results possess χ^2 values that approach one if the 22.3-GPa pressure results are excluded. The conclusions are robust in the sense that three completely independent measurement approaches have been incorporated, lending further confidence to the model comparison results. It is interesting that models which are very successful at predicting the temperatures over the 30–90-GPa range still disagree with the 22.3-GPa measurements when the gas gun results are averaged with the Z results. The discrepancy at 22.3 GPa is strongly influenced by the single Z904N19 measurement and we therefore believe that further measurements are needed to ascertain whether this discrepancy is due to measurement errors or if it implies ongoing model refinements are needed.

It is also interesting to examine the impact of these results for applications. Inertial confinement fusion (ICF) capsule implosions are predicted⁴⁴ to reach higher final fuel density and therefore achieve higher gain if the more compressible EOS models are employed. Recent thermonuclear ignition calculations⁴⁵ use an EOS that is stated to be intermediate between the softer and stiffer EOS models. Unfortunately, a systematic evaluation of the EOS influence on ICF ignition and gain has not yet been published, as far as we know. The present results are incompatible with the soft EOS models and therefore do not support the more optimistic predictions obtained with those models. However, these results provide improved certainty in the D_2 EOS and therefore may pro-

mote the likelihood of ignition on the National Ignition Facility, since reducing the EOS uncertainty could allow directing the facility tuning experiments toward other remaining issues.⁴⁶

In contrast to ICF, systematic evaluations of the D_2 EOS influence on giant planets have been performed. Saumon and Guillot¹⁴ constructed models for the internal structure of Jupiter and Saturn using different EOS models and the observational constraints provided by measurements of the planet radius, mass, rotational period, and gravitational moment. Models were employed that spanned the range of data found in the available experiments.^{19–21,23–26} They used several linear mixing models, including a model (LM-A, B) similar to Ref. 4, a model with a revised treatment of the metallic fluid (LM-SOCP), and a model with explicit introduction of D_4 chains (LM-H4). In addition, they used a version of the SESAME EOS⁵ modified to improve agreement with low-pressure measurements (Sesame- p) and the SCVH chemical model.⁸ They found that Jupiter was particularly sensitive to the EOS. Comparisons of the weighted mean temperature as a function of pressure with results from five of the EOS models published in Ref. 14 are shown in Fig. 14. QMD calculations¹¹ are superimposed in order to help relate these models to the results shown in Fig. 12. The softest model, linear mixing A and B (LM-AB), is obviously incompatible with the temperature measurements, as with the softer models displayed in Fig. 12. The goodness of fit for these models is quantitatively evaluated using χ^2 in Table III. The individual measurements exclude the soft LM-A,B models but cannot distinguish between the stiffer (SCVH, Sesame- p , LM-H4, LM-SOCP) models. The tighter constraints provided by the weighted mean and global mean show that only the Sesame- p model approaches the fit quality obtained in the comparisons described above with the Desjarlais QMD,¹¹ Collins *et al.* QMD,¹² and tight-binding QMD⁷ models. On the other hand, the χ^2 statistic for the LM-H4 model compared with the weighted mean temperature over the 30–90-GPa range is 2.3, making it less likely but still a statistical possibility.

This is significant because the results in Saumon and Guillot¹⁴ indicate that the core of Jupiter has mass less than approximately three Earth masses if the Sesame- p model is used to represent the EOS. The implication of the present results together with the Ref. 14 analysis is that the core mass of Jupiter is too small to be consistent with formation by accretion around a massive core. An alternative suggested in Ref. 14 is that the core and outer gaseous envelope may have mixed after formation.

In summary, the work presented here provides measurements of pressure steadiness, emissivity, and temperature in singly shocked D_2 at pressures between 22–90 GPa. The temperature measurements provide strong evidence supporting *ab initio* D_2 EOS models that predict a maximum compressibility of approximately four. The measurements preclude the softer EOS models that predict approximately sixfold compressions. The conclusions are the same even if global mean temperature values are constructed from the existing data provided by gas gun, laser, and magnetic flyer experiments. Finally, we note that the present work focused entirely on conditions in singly shocked D_2 along the Hugo-

niot. However, high-quality data exist for multiply-shocked conditions as well (Figs. 1 and 2). Work is in progress to infer temperature from these off-Hugoniot conditions. These conditions are likely to be helpful in further EOS model evaluations and in understanding giant planet interiors.

ACKNOWLEDGMENTS

We thank the Z flyer plate, accelerator, diagnostics, mate-

rials processing, target, and fabrication teams for invaluable and dedicated technical assistance. L. P. Mix, R. Hahn, and L. Nielsen-Weber provided data processing assistance. We are grateful to D. H. Dolan for carefully reviewing the manuscript and to R. J. Leeper, T. A. Mehlhorn, C. Deeney, and M. K. Matzen for support and encouragement. Sandia is a multiprogram laboratory operated by Sandia Corporation, a Lockheed Martin Co., for the U.S. Department of Energy under Contract No. DE-AC04-94AL85000.

-
- ¹Y. M. Gupta and S. M. Sharma, *Science* **277**, 909 (1997).
²See Special Issue on Hydrogen at High Pressure, *High Press. Res.* **16**, 281 (2000).
³W. J. Nellis, *Phys. Rev. Lett.* **89**, 165502 (2002); *Astrophys. Space Sci.* **298**, 141 (2005).
⁴M. Ross, *Phys. Rev. B* **58**, 669 (1998).
⁵G. I. Kerley, *Phys. Earth Planet. Inter.* **6**, 78 (1972); also (private communication).
⁶D. A. Young, *High Press. Res.* **16**, 389 (2000).
⁷T. J. Lenosky, J. D. Kress, and L. A. Collins, *Phys. Rev. B* **56**, 5164 (1997); (private communication).
⁸D. Saumon, G. Chabrier, and H. M. Van Horn, *Astrophys. J., Suppl. Ser.* **99**, 713 (1995); D. Saumon, G. Chabrier, D. J. Wagner, and X. Xie, *High Press. Res.* **16**, 331 (2000).
⁹R. Redmer, *High Press. Res.* **16**, 345 (2000).
¹⁰T. J. Lenosky, S. R. Bickham, J. D. Kress, and L. A. Collins, *Phys. Rev. B* **61**, 1 (2000).
¹¹M. P. Desjarlais, *Phys. Rev. B* **68**, 064204 (2003).
¹²L. A. Collins, S. R. Bickham, J. D. Kress, S. Mazevet, T. J. Lenosky, N. J. Troullier, and W. Windl, *Phys. Rev. B* **63**, 184110 (2001).
¹³M. P. Desjarlais, J. D. Kress, and L. A. Collins, *Phys. Rev. E* **66**, 025401(R) (2002); S. Mazevet, M. P. Desjarlais, L. A. Collins, J. D. Kress, and N. H. Magee, *ibid.* **71**, 016409 (2005).
¹⁴D. Saumon and T. Guillot, *Astrophys. J.* **609**, 1170 (2004).
¹⁵W. B. Hubbard, *Nature (London)* **431**, 32 (2004); D. Saumon and T. Guillot, *Astrophys. Space Sci.* **298**, 135 (2005); G. Chabrier, D. Saumon, and C. Winisdoerffer, *ibid.* **307**, 263 (2007).
¹⁶J. Lindl, *Phys. Plasmas* **2**, 3933 (1995).
¹⁷S. T. Weir, A. C. Mitchell, and W. J. Nellis, *Phys. Rev. Lett.* **76**, 1860 (1996).
¹⁸N. C. Holmes, M. Ross, and W. J. Nellis, *Phys. Rev. B* **52**, 15835 (1995).
¹⁹L. B. Da Silva, P. Celliers, G. W. Collins, K. S. Budil, N. C. Holmes, T. W. Barbee, Jr., B. A. Hammel, J. D. Kilkenny, R. J. Wallace, M. Ross, R. Cauble, A. Ng, and G. Chiu, *Phys. Rev. Lett.* **78**, 483 (1997).
²⁰G. W. Collins, L. B. Da Silva, P. Celliers, D. M. Gold, M. E. Foord, R. J. Wallace, A. Ng, S. V. Weber, K. S. Budil, and R. Cauble, *Science* **281**, 1178 (1998).
²¹R. Cauble, P. M. Celliers, G. W. Collins, L. B. Da Silva, D. M. Gold, M. E. Foord, K. S. Budil, R. J. Wallace, and A. Ng, *Astrophys. J., Suppl. Ser.* **127**, 267 (2000).
²²A. N. Mostovych, Y. Chan, T. Lehecha, A. Schmitt, and J. D. Sethian, *Phys. Rev. Lett.* **85**, 3870 (2000); *Phys. Plasmas* **8**, 2281 (2001).
²³M. D. Knudson, D. L. Hanson, J. E. Bailey, C. A. Hall, J. R. Asay, and W. W. Anderson, *Phys. Rev. Lett.* **87**, 225501 (2001).
²⁴M. D. Knudson, D. L. Hanson, J. E. Bailey, C. A. Hall, and J. R. Asay, *Phys. Rev. Lett.* **90**, 035505 (2003).
²⁵M. D. Knudson, D. L. Hanson, J. E. Bailey, C. A. Hall, J. R. Asay, and C. Deeney, *Phys. Rev. B* **69**, 144209 (2004).
²⁶G. V. Boriskov, A. I. Bykov, R. Ilkaev, V. D. Selemir, G. V. Simakov, R. F. Trunin, V. D. Urlin, A. N. Shuikin, and W. J. Nellis, *Phys. Rev. B* **71**, 092104 (2005).
²⁷T. R. Boehly, D. G. Hicks, P. M. Celliers, T. J. B. Collins, R. Earley, J. H. Eggert, D. Jacobs-Perkins, S. J. Moon, E. Vianello, D. D. Meyerhofer, and G. W. Collins, *Phys. Plasmas* **11**, L49 (2004).
²⁸N. C. Holmes, *Rev. Sci. Instrum.* **66**, 2615 (1995).
²⁹G. W. Collins, P. M. Celliers, L. B. Da Silva, R. Cauble, D. M. Gold, M. E. Foord, N. C. Holmes, B. A. Hammel, R. J. Wallace, and A. Ng, *Phys. Rev. Lett.* **87**, 165504 (2001).
³⁰P. M. Celliers, G. W. Collins, L. B. Da Silva, D. M. Gold, R. Cauble, R. J. Wallace, M. E. Foord, and B. A. Hammel, *Phys. Rev. Lett.* **84**, 5564 (2000).
³¹J. E. Bailey, A. L. Carlson, R. L. Morrison, and Y. Maron, *Rev. Sci. Instrum.* **61**, 3075 (1990).
³²J. E. Bailey, J. Asay, M. Bernard, A. L. Carlson, G. A. Chandler, C. A. Hall, D. Hanson, R. Johstone, P. Lake, and J. Lawrence, *J. Quant. Spectrosc. Radiat. Transf.* **65**, 31 (2000).
³³G. Dunham, J. E. Bailey, A. Carlson, P. Lake, and M. D. Knudson, *Rev. Sci. Instrum.* **75**, 928 (2004).
³⁴L. M. Barker and R. E. Hollenbach, *J. Appl. Phys.* **43**, 4669 (1972).
³⁵M. K. Matzen, *Phys. Plasmas* **4**, 1519 (1997); R. B. Spielmann, C. Deeney, G. A. Chandler *et al.*, *ibid.* **5**, 2105 (1998); M. K. Matzen, M. A. Sweeney, R. G. Adams *et al.*, *ibid.* **12**, 055503 (2005).
³⁶M. D. Knudson, R. W. Lemke, D. B. Hayes, C. A. Hall, C. Deeney, and J. R. Asay, *J. Appl. Phys.* **94**, 4420 (2003).
³⁷R. W. Lemke, M. D. Knudson, C. A. Hall, T. A. Haill, M. P. Desjarlais, J. R. Asay, and T. A. Mehlhorn, *Phys. Plasmas* **10**, 1092 (2003).
³⁸R. W. Lemke, M. D. Knudson, A. C. Robinson, T. A. Haill, K. W. Struve, J. R. Asay, and T. A. Mehlhorn, *Phys. Plasmas* **10**, 1867 (2003).
³⁹D. L. Hanson, R. R. Johnson, M. D. Knudson, J. R. Asay, C. A. Hall, J. E. Bailey, and R. J. Hickman, in *Shock Compression of Condensed Matter – 2001*, AIP Conf. Proc. No. 620, edited by M. D. Furnish, N. N. Thadhani, and Y. Horie (AIP, New York,

- 2002), p. 1141; D. L. Hanson, M. D. Knudson, J. R. Asay, C. A. Hall, J. E. Bailey, R. W. Lemke, J-P. Davis, R. B. Spielman, B. V. Oliver, and D. B. Hayes, in *Inertial Fusion Sciences and Applications 2001*, edited by K. A. Tanaka, D. D. Meyerhofer, and J. Meyer-ter-Vehn (Elsevier, Paris, 2002), p. 1091.
- ⁴⁰K. Cochrane, J. E. Bailey, P. Lake, and A. Carlson, *Appl. Opt.* **40**, 150 (2001).
- ⁴¹G. Kresse and J. Furthmuller, *Phys. Rev. B* **54**, 11169 (1996), and References therein.
- ⁴²R. L. Coldwell and G. J. Bamford, *The Theory and Operation of Spectral Analysis Using ROBFIT* (AIP, New York, 1991).
- ⁴³P. R. Bevington and D. K. Robinson, *Data Reduction and Error Analysis for the Physical Sciences* (Mcgraw-Hill, New York, 1992).
- ⁴⁴T. R. Dittrich, S. W. Haan, M. M. Marinak, S. M. Pollaine, D. E. Hinkel, D. H. Munro, C. P. Verdon, G. L. Strobel, R. McEachern, R. C. Cook, C. C. Roberts, D. C. Wilson, P. A. Bradley, L. R. Foreman, and W. S. Varnum, *Phys. Plasmas* **6**, 2164 (1999).
- ⁴⁵S. W. Haan, M. C. Herrmann, T. R. Dittrich, A. J. Fetterman, M. M. Marinak, D. H. Munro, S. M. Pollaine, J. D. Salmonson, G. L. Strobel, and L. J. Suter, *Phys. Plasmas* **12**, 056316 (2005).
- ⁴⁶R. E. Olson, *Fusion Technol.* **38**, 6 (2000); D. S. Clark, S. W. Haan, and J. Salmonson, *Phys. Plasmas* **15**, 056305 (2008).